





Article

The Impact of Full-Scale Substitution of Ca^{2+} with Ni^{2+} Ions on Brushite's Crystal Structure and Phase Composition

Mazen Alshaaer ^{1,2,*}, Khalil Issa ^{3,*}, Ahmed S. Afify ⁴, Moustapha E. Moustapha ⁵, Abdulaziz A. Alanazi ⁵, Ammar Elsanousi ¹ and Talal F. Qahtan ¹

¹ Department of Physics, College of Science and Humanities in Al-Kharj, Prince Sattam Bin Abdulaziz University, Al-Kharj 11942, Saudi Arabia; a.elsanousi@psau.edu.sa (A.E.); tfqahtan@gmail.com (T.F.Q.)

² GeoBioTec Research Centre, Campus de Santiago, University of Aveiro, 3810-193 Aveiro, Portugal

³ Orthopedics Unit, Faculty of Medicine and Health Sciences, An-Najah National University, Nablus 00972, Palestine

⁴ Department of Basic Sciences, Higher Institute of Engineering and Automotive Technology and Energy, New Heliopolis 11829, Egypt; ahmed.afify@polito.it

⁵ Department of Chemistry, College of Science and Humanities in Al-Kharj, Prince Sattam Bin Abdulaziz University, Al-Kharj 11942, Saudi Arabia; m.moustapha@psau.edu.sa (M.E.M.); abdulaziz.alanazi@psau.edu.sa (A.A.A.)

* Correspondence: mazen.alshaaer@yahoo.com or m.alshaaer@psau.edu.sa (M.A.); k.issa@najah.edu (K.I.)

Abstract: Because the impact of the full-scale substitution of Ca^{2+} in brushite ($\text{CaHPO}_4 \cdot 2\text{H}_2\text{O}$) with Ni^{2+} ions has never been systematically explored, it is the focus of this investigation, as it holds potential for use in $\text{Ca}_x\text{Ni}_{1-x}\text{HPO}_4 \cdot n\text{H}_2\text{O}$ production. These biomaterials have many beneficial characteristics that can be modified to suit diverse applications, including bone tissue regeneration and pharmaceuticals. For the present study, $\text{NaH}_2\text{PO}_4 \cdot 2\text{H}_2\text{O}$, $\text{Ca}(\text{NO}_3)_2 \cdot 4\text{H}_2\text{O}$, and $\text{Ni}(\text{NO}_3)_2 \cdot 6\text{H}_2\text{O}$ were used in various molar concentrations to obtain the required starting solutions. Previous studies have shown that adding Ni ions in the initial solution below 20% results in the precipitation of monophasic brushite with slight changes in the crystal structure. However, this study confirms that when the Ni ions substitution increases to 20%, a mixture of phases from both brushite and hexaaquanickel(II) hydrogenphosphate monohydrate HNiP ($\text{Ni}(\text{H}_2\text{O})_6 \cdot \text{HPO}_4 \cdot \text{H}_2\text{O}$) is formed. The results confirm that the full replacement (100%) of Ca ions by Ni ions results in a monophasic compound solely comprising orthorhombic HNiP nanocrystals. Therefore, a novel technique of HNiP synthesis using the precipitation method is introduced in this research work. These materials are subsequently analyzed utilizing powder X-ray diffraction (XRD), X-ray photoelectron spectroscopy (XPS), thermogravimetric analysis (TGA), and scanning electron microscopy (SEM). The obtained results confirm that the material microstructure is controlled by the Ni/Ca ratio in the starting solution and can be modified to obtain the desired characteristics of phases and crystals.

Keywords: brushite; hexaaquanickel(II) hydrogen phosphate monohydrate; biomaterials; XPS; kidney stone



Citation: Alshaaer, M.; Issa, K.; Afify, A.S.; Moustapha, M.E.; Alanazi, A.A.; Elsanousi, A.; Qahtan, T.F. The Impact of Full-Scale Substitution of Ca^{2+} with Ni^{2+} Ions on Brushite's Crystal Structure and Phase Composition. *Crystals* **2022**, *12*, 940. <https://doi.org/10.3390/cryst12070940>

Academic Editors: Aleksey Zarkov, Aivaras Kareiva and Loreta Tamasauskaitė-Tamasiunaite

Received: 21 May 2022

Accepted: 30 June 2022

Published: 4 July 2022

Publisher's Note: MDPI stays neutral with regard to jurisdictional claims in published maps and institutional affiliations.



Copyright: © 2022 by the authors. Licensee MDPI, Basel, Switzerland. This article is an open access article distributed under the terms and conditions of the Creative Commons Attribution (CC BY) license (<https://creativecommons.org/licenses/by/4.0/>).

1. Introduction

Owing to their beneficial mineralogical and biochemical characteristics, calcium phosphates (CaPs) already have diverse applications, including those in the environmental sciences and the field of engineering. However, their similarity with the mineral phases present in osseous tissue—as well as a low toxicity, high bioactivity, and excellent biocompatibility—makes them particularly useful candidates for medical applications [1–4]. Presently, CaPs serve as precursors for biocements and bioceramics, to be used in medicine and dentistry, and to obtain other types of advanced materials [4,5]. Available evidence further indicates that CaPs can be adopted for drug delivery or bone tissue engineering [5,6], in fertilizers [7], and in the construction industry [8–10].

Nickel is one of the trace elements in the human body, where the average amount in a healthy individual is about 10 mg [11,12]. The concentration of nickel per liter of serum is about 0.2 µg/L in a normal population [11]. Nickel is known to be harmful to human health, causing cancer, inflammation, skin allergies, lung fibrosis, asthma, and kidney diseases [13]. Yet later, it was found that nickel toxicity depends on the amount of the dose so that it can be used in vivo under certain conditions and modifications. In view of these facts, nickel has been adopted for biomedical applications involving stainless steel (15% Ni) or shape-memory alloys such as nitinol (50% Ni) [14,15]. Such Nickel-based alloys are now used in biomedical implants for clinical application [12].

Nickel ions and other d-block elements (Co, Cu, V, Ti, Cr) exhibit one very important property, which is the stabilization of HIF-1 α ; therefore, they can induce cellular VEGF secretion by creating intracellular hypoxia mimicking conditions. Nickel-doped nHAp having different percentages of Ni (1%, 5%, and 10% *w/w*) [12] is a proangiogenic–osteogenic material that could be used in bone tissue engineering, as doped samples proved bone-cell compatible and osteoconductive. Analysis showed that Ni²⁺ doped nHAp samples were potent inducers of the cellular Vascular Endothelial Growth Factor (VEGF), the expression of VEGF being directly proportional to the doping concentration of Ni²⁺ [12].

Several studies indicate that dicalcium phosphate dehydrate (DCPD)—commonly known as brushite, with the chemical formula CaHPO₄·2H₂O—is one of the most widely used CaPs [8,11]. This mineral acts as a precursor of hydroxyapatite (HA), bone cement, and bioceramics. Hence, the brushite encountered in mineralized tissues can be useful in medicine, especially in bone cement formulations [16]. It shows high stability in environments characterized by pH 4.0–6.5 and temperatures below 60 °C [17–20]. Moreover, as it is usually metastable at pH ~7.4, it can be quickly resorbed in the human body to aid in bone remodeling [21–23].

The influence of ionic substitution on the morphology, structure, synthesis and hydrolysis process of brushite has been investigated [1]. The results of structural refinements indicate that the range of possible substitutions can reach different values based on the doped ions. This study showed that the Sr substitution can reach up to about 38%, whereas it is quite limited for Co, Mn, and Zn. A previous study [24] has shown the most complete incorporation of Ni²⁺ to the solid phase of brushite up to 15%. However, for larger Ni²⁺ concentrations in the initial solution, a mixture of phases has been detected [24,25].

Such findings have prompted us to study the crystal morphology, thermal properties, chemical composition, phases, and mineralogy of the produced compounds when Ca²⁺ in brushite is gradually substituted or replaced (from 20% to 100%) by Ni²⁺. The findings fill an important research gap and may prove valuable for mineral synthesis to derive biomaterials for a variety of applications in the bone tissue engineering and the pharmaceutical industry.

2. Experimental Methodology

2.1. Materials

Sodium dihydrogen orthophosphate dihydrate (NaH₂PO₄·2H₂O) was purchased from Techno Pharmchem, India; while calcium nitrate tetrahydrate (Ca(NO₃)₂·4H₂O) and nickel (II) nitrate hexahydrate (Ni(NO₃)₂·6H₂O) were procured from LOBA Chemie, India. Distilled water (0.055 µS/cm) was prepared using a water purification system (PURELAB option-Q, ELGA, Oxford, UK). A digital analytical balance (EX324N, OHAUS, Parsippany, NJ, USA) and a magnetic stirrer (ISOTEMP, Fisher Scientific, Shanghai, China) were used when required.

2.2. Synthesis of Ca_xNi_{1-x}HPO₄·nH₂O Compounds

A series of six Ca_xNi_{1-x}HPO₄·nH₂O compounds (with *x* = 0, 2, 4, 5, 6, and 10) was synthesized at room temperature (RT) based on the reaction given in Equation (1), which called for the use of Na₂HPO₄·2H₂O, Ca(NO₃)₂·4H₂O and Ni(NO₃)₂·6H₂O 0.5 mol/L solutions in the molar proportions provided in Table 1.



Table 1. Molar proportions of $\text{NaH}_2\text{PO}_4 \cdot 2\text{H}_2\text{O}$, $\text{Ca}(\text{NO}_3)_2 \cdot 4\text{H}_2\text{O}$, and $\text{Ni}(\text{NO}_3)_2 \cdot 6\text{H}_2\text{O}$, as well as Ni/Ca molar ratios used for the synthesis of $\text{Ca}_x\text{Ni}_{1-x}\text{HPO}_4 \cdot n\text{H}_2\text{O}$ compounds.

Product ID	$\text{NaH}_2\text{PO}_4 \cdot 2\text{H}_2\text{O}$	$\text{Ca}(\text{NO}_3)_2 \cdot 4\text{H}_2\text{O}$	$\text{Ni}(\text{NO}_3)_2 \cdot 6\text{H}_2\text{O}$	Ni/Ca Molar Ratio
BNi0	1	1	0	0
BNi2	1	0.8	0.2	0.25
BNi4	1	0.6	0.4	0.67
BNi5	1	0.5	0.5	1.0
BNi6	1	0.4	0.6	1.5
BNi10	1	0	1	-

To obtain pure brushite (denoted in Table 1 as BNi0), 100 mL of $\text{Ca}(\text{NO}_3)_2 \cdot 4\text{H}_2\text{O}$ solution was added at the ≈ 2 mL/min flow rate to the $\text{Na}_2\text{HPO}_4 \cdot 2\text{H}_2\text{O}$ solution using a glass funnel with a glass stopcock while stirring at 450 rpm until a 1.0 Ca/P molar ratio was achieved (which typically took about 60 min). The resulting solution was stirred at RT for 60 min to ensure that it was fully homogenized, after which the pH was adjusted to 6–6.5 by adding ammonia solution (≈ 15 mol/L, Labochemie, Mumbai, India) as required. The aim was to obtain a white precipitate that was then vacuum filtered using a Buchner funnel and a qualitative filter paper (45 μm , $\varnothing 12$ cm, Double Rings, Shanghai, China). The filter cake was first washed three times with deionized water, which was followed by three washes in ethanol to prevent agglomeration [26–28]. Finally, the sample was placed on a watch glass and was left to dry in an oven set at 40 °C for one week (ED53/E2, Binder, Tuttlingen, Germany) [29].

To obtain BNi2, BNi4, BNi5, and BNi6 compounds, the $\text{Ca}(\text{NO}_3)_2 \cdot 4\text{H}_2\text{O}$ and $\text{Ni}(\text{NO}_3)_2 \cdot 6\text{H}_2\text{O}$ solutions were mixed in the molar ratios outlined in Table 1, after which 100 mL of the resulting solution was added at the ≈ 2 mL/min flow rate to 100 mL of $\text{Na}_2\text{HPO}_4 \cdot 2\text{H}_2\text{O}$ solution as described above. For BNi10, the same process was performed after mixing $\text{NaH}_2\text{PO}_4 \cdot 2\text{H}_2\text{O}$ and $\text{Ni}(\text{NO}_3)_2 \cdot 6\text{H}_2\text{O}$.

2.3. Characterization Techniques

The obtained BNi0–BNi10 samples were subjected to powder diffraction phase analysis using a Shimadzu XRD diffractometer-6000 (Japan) with a cobalt tube and a 2-theta scanning range of 10–60° at a 2°/min scan rate. Product morphology was established via scanning electron microscopy with the Inspect F50 (The Netherlands) apparatus. An XPS system (Thermo K Alpha spectrometer, Thermo Fisher Scientific, Waltham, MA, USA) was used to conduct X-ray photoelectron spectroscopy to determine the surface chemistry and conduct elemental analysis of the samples. Finally, a thermogravimetric (TGA) analyzer (TG 209 F1 Libra, Netzsch, Selb, Germany) served to ascertain the mass loss (≈ 100 mg) resulting from heating each product from 40 to 600 °C, at 5 °C min^{−1} increments under a helium atmosphere. An FT-IR spectrometer (Perkin–Elmer system 2000) was used for recording FTIR spectra in the range of 4000–400 cm^{−1}.

3. Results and Discussion

3.1. Mineralogical and Microstructural Analysis

The XRD patterns produced by all samples, including standard brushite ($\text{CaHPO}_4 \cdot 2\text{H}_2\text{O}$) and hexaaquanickel(II) hydrogenphosphate monohydrate ($\text{Ni}(\text{H}_2\text{O})_6 \cdot \text{HPO}_4 \cdot \text{H}_2\text{O}$) (HNiP), are presented in Figure 1. The qualitative mineralogical analysis confirmed that after mixing $\text{NaH}_2\text{PO}_4 \cdot 2\text{H}_2\text{O}$ and $\text{Ca}(\text{NO}_3)_2 \cdot 4\text{H}_2\text{O}$ solutions with a Ca:P molar ratio of 1:1 (Table 1), pure brushite (BNi0) is precipitated. Moreover, after nucleation, its crystals grow proportionately to the three major crystallographic planes, i.e., (020), (12-1), and (14-1). In addition, all

peaks identified in the pattern produced by BNi0 are indicative of brushite's monoclinic structure [19,30], while the peak at 11.7° 2-theta suggests that crystal growth primarily progresses along the (020) plane [31].

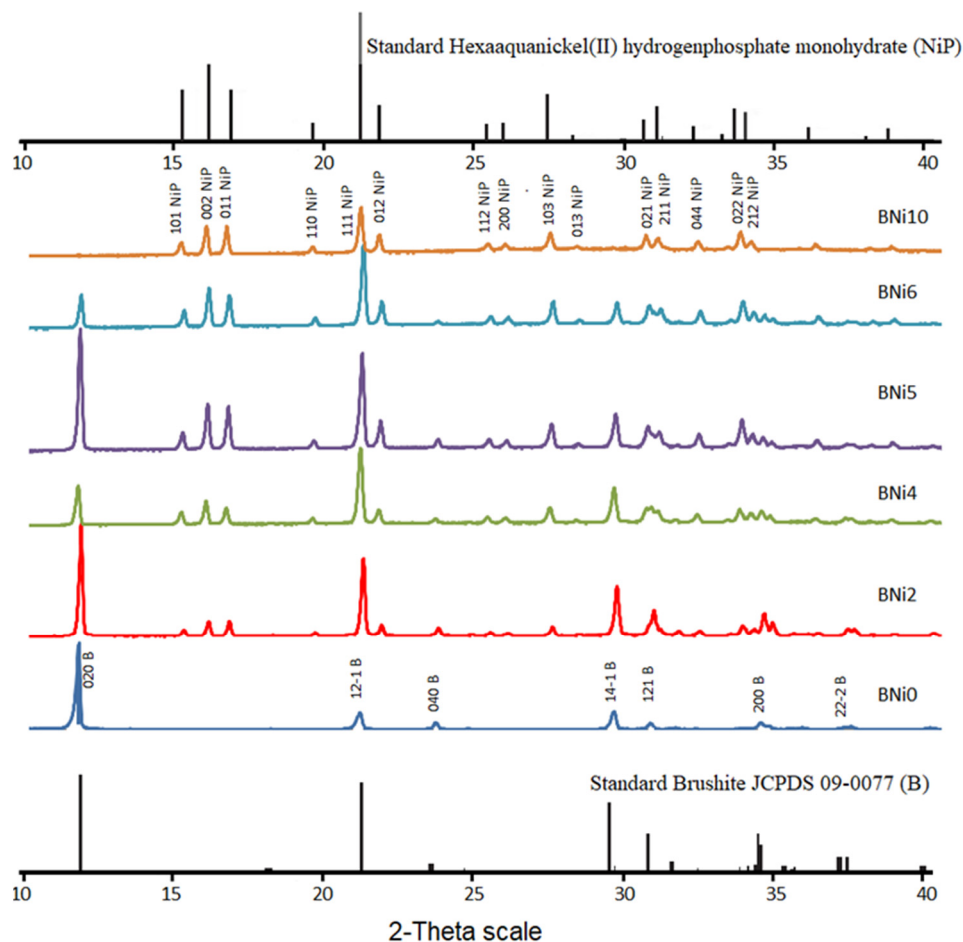


Figure 1. XRD patterns of the $\text{Ca}_x\text{Ni}_{1-x}\text{HPO}_4 \cdot n\text{H}_2\text{O}$ compounds synthesized under the conditions provided in Table 1.

In addition to the growth of XRD peaks corresponding to HNiP, all the main brushite peaks can be identified in the pattern, BNi2, and show higher intensity than in the BNi0 spectrum, especially for peaks associated with the (020), (121), and (141) planes [32,33].

The patterns produced by BNi2 to BNi6 (corresponding to the Ni/Ca molar ratio of 0.25 to 1.5), as expected, indicate that a greater proportion of Ca is substituted by Ni, while hexaaquanickel(II) hydrogenphosphate monohydrate ($\text{Ni}(\text{H}_2\text{O})_6 \cdot \text{HPO}_4 \cdot \text{H}_2\text{O}$) (HNiP) also began to precipitate. The planes corresponding to $\text{Ni}(\text{H}_2\text{O})_6 \cdot \text{HPO}_4 \cdot \text{H}_2\text{O}$ —(101), (002), (011), (111) and (103)—are thus observed. The XRD patterns further show that as the Ni/Ca molar ratio increases, so does the HNiP peak intensity. Finally, the pattern produced by BNi10 (with the Ni/P ratio of 1.0) confirms the presence of pure HNiP with an orthorhombic crystal structure, as seen in Figure 1.

Figure 2 provides the SEM images of brushite (BNi0), along with those of biphasic compounds (BNi2, BNi4, and BNi6) based on different Ni/Ca molar ratios. The SEM image of pure HNiP ($\text{Ni}(\text{H}_2\text{O})_6 \cdot \text{HPO}_4 \cdot \text{H}_2\text{O}$; BNi10) is presented in Figure 3.

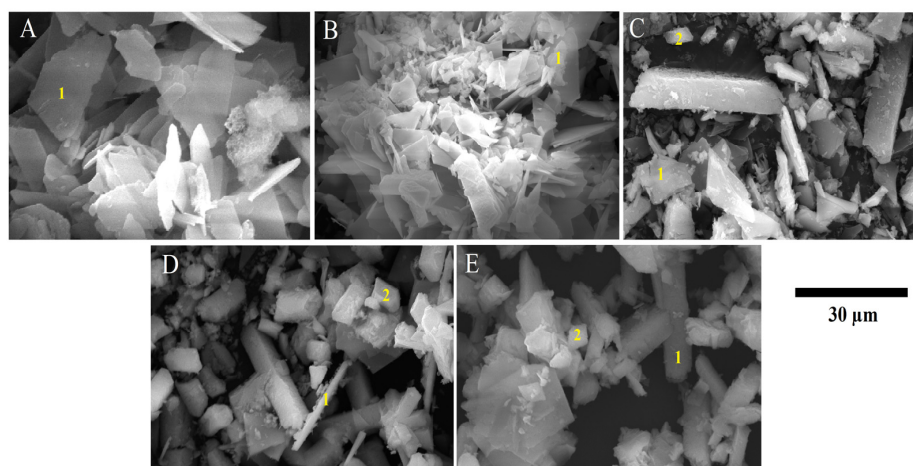


Figure 2. SEM images of $\text{Ca}_x\text{Ni}_{1-x}\text{HPO}_4 \cdot n\text{H}_2\text{O}$ compounds (labeled using product names provided in Table 1 and obtained with the same magnification): (A) BNi0; (B) BNi2; (C) BNi4; (D) BNi5, and (E) BNi6. (Point 1—brushite crystals, Point 2—hexaaquanickel(II) hydrogenphosphate monohydrate).

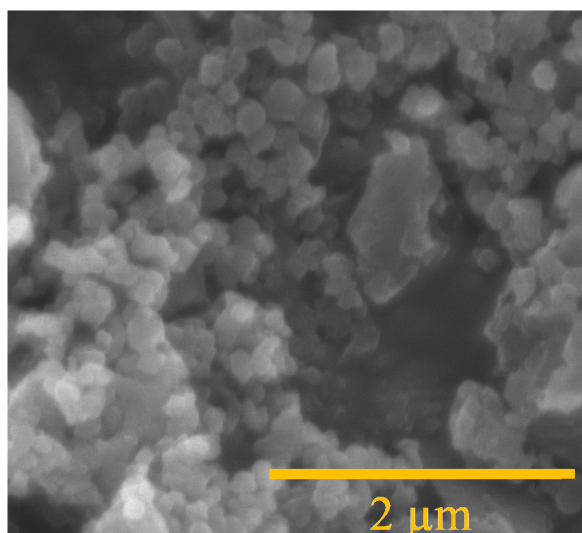


Figure 3. SEM images of hexaaquanickel(II) hydrogenphosphate monohydrate crystals ($\text{Ni}(\text{H}_2\text{O})_6 \cdot \text{HPO}_4 \cdot \text{H}_2\text{O}$ (HNiP); product name BNi10).

As can be seen at Point 1 in Figure 2A (pertaining to BNi0 with the Ca/P molar ratio 1.0), the precipitation of pure brushite results in plate-like crystals, as expected for the solution pH used in this work [17,18]. The dimensions of these plate-like crystals are $\approx 500 \text{ nm} \times 15 \mu\text{m} \times 30 \mu\text{m}$, which is comparable to those obtained by other authors [10,34]. Moreover, flat-plate morphology is a typical crystal structure for precipitated brushite [35]. It is evident from Point 1 in Figure 2B that as Ca replacement with Ni intensifies due to the increase in the Ni/Ca molar ratio, the length of brushite crystals in the (020) direction decreases, ranging between ≈ 5 and $\approx 20 \mu\text{m}$. Finally, as seen in Figure 2B–E—depicting a biphasic compound—brushite crystals (Point 1) of different sizes are formed alongside HNiP crystals (Point 2).

BNi10 is depicted in Figure 3, which confirms that the full replacement of Ca by Ni results in a monophasic compound made up only of orthorhombic HNiP nanocrystals. Thus, the findings yielded by SEM analysis confirm those obtained via the XRD shown in Figure 1.

Rietveld refined unit cell parameters for brushite and HNiP materials are presented in Tables 2 and 3. As evidenced by the tabulated data, the values of unit cell parameters related to brushite increase as the Ni/Ca molar ratio increases from 0 to 1; hence, brushite

is the dominant phase formed. Yet, when the Ni/Ca molar ratio exceeds 1, the brushite unit cell parameters decrease. Similarly, the parameters pertaining to the HNiP unit cell increase as the Ni/Ca molar ratio increases from 0.25 to 1 (Table 3). Still, the unit cell dimensions of pure HNiP are larger than those characterizing the standard unit cell.

Table 2. The unit cell parameters for brushite are derived from the XRD scans (Rietveld refinement).

Product ID	Brushite wt %	a (Å)	b (Å)	c (Å)	β o	V (Å ³)
Standard Brushite	100	5.812	15.18	6.239	116.43	492.91
BNi0	100	5.8145	15.1693	6.2399	116.43	492.8455
BNi2	93	5.81143	15.17852	6.23839	116.43	492.7654
BNi4	25.5	5.8195	15.19959	6.24705	116.43	494.8206
BNi5	34.5	5.82386	15.21097	6.25173	116.43	495.9334
BNi6	14.6	5.81326	15.18328	6.24035	116.43	493.2301
BNi10	0	-	-	-	-	-

Table 3. The unit cell parameters for HNiP (product name BNi10) are derived from XRD scans (Rietveld refinement).

Product ID	Brushite wt %	a (Å)	b (Å)	c (Å)	V (Å ³)
Standard HNiP	100	6.916	6.1032	11.1679	471.394
BNi0	0	-	-	-	-
BNi2	7	6.91997	6.09953	11.14389	470.3676
BNi4	74.5	6.93074	6.11028	11.17562	473.2737
BNi5	65.5	6.94044	6.11663	11.18034	474.629
BNi6	85.4	6.9211	6.10223	11.16156	471.3989
BNi10	100	6.9356	6.10915	11.17447	473.4692

The FT-IR spectrum of the $\text{Ca}_x\text{Ni}_{1-x}\text{HPO}_4 \cdot n\text{H}_2\text{O}$ compounds is shown in Figure 4. The broad absorption peak between 3500 and 2400 cm^{-1} is due to O-H stretching vibration [36]. The P-O-P asymmetric stretching vibration band was observed at 983 cm^{-1} as a result of P=O stretching vibrations; other bands at 654 and 568 cm^{-1} may be attributed to (H-O)P=O for acid phosphates [36,37]. Another two peaks were observed at 3470 and 1640 cm^{-1} , indicating the existence of water, and their intensity decreased along with the decreasing trend in brushite contents in the samples (BNi2, BNi4, BNi5, and BNi6), whereas the BNi6 and BNi10 spectra reflected an absence of water [38]. On the other hand, the samples showed new peaks at 1645 and 1432 cm^{-1} , which were respectively indexed to O-H and P-O-bending vibrations, owing to the presence of Ni and its intensity, which reached a maximum in samples BNi6 and BNi10 [39,40].

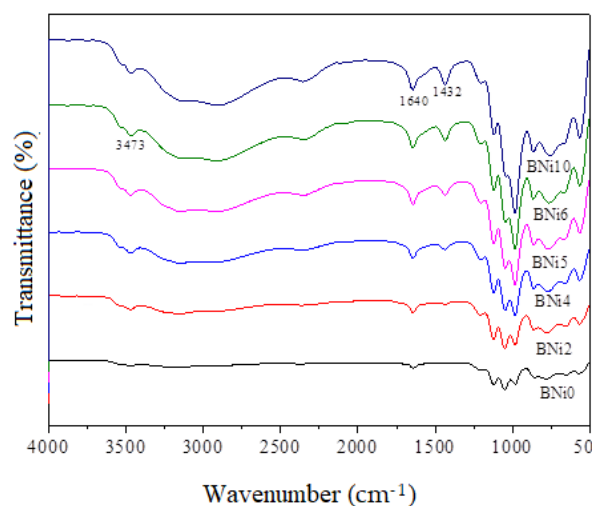


Figure 4. FT-IR spectrum of $\text{Ca}_x\text{Ni}_{1-x}\text{HPO}_4 \cdot n\text{H}_2\text{O}$ compounds.

3.2. Elemental and Chemical Composition of $\text{Ca}_x\text{Ni}_{1-x}\text{HPO}_4 \cdot n\text{H}_2\text{O}$ Compounds

The prepared samples were subjected to XPS analysis to appraise how the Ni/Ca ratio present in the starting solution affected the surface chemistry and chemical state of P, Ca, and Ni as the main constituents of the synthesized $\text{Ca}_x\text{Ni}_{1-x}\text{HPO}_4 \cdot n\text{H}_2\text{O}$ compounds; these findings are presented in Figure 5. As previously noted, the Ni/Ca ratio affects the degree of substitution of Ca with Ni in brushite as well as the precipitation of HNiP (when higher Ni/Ca ratios are used). The peaks corresponding to the Ni 2p orbital are visible in the XPS spectra of BNi2 to BNi10, and their intensity progressively increases, whereas the intensity of the Ca 2s and Ca 2p peaks decreases almost proportionally with the increase in the Ni/Ca ratio. Meanwhile, the intensity of the P 2s peaks remains nearly constant. This means that the intensity of P, Ca, and Ni peaks depend on the degree of Ca replacement with Ni as well as on the amount of the precipitated HNiP (for higher Ni/Ca ratios).

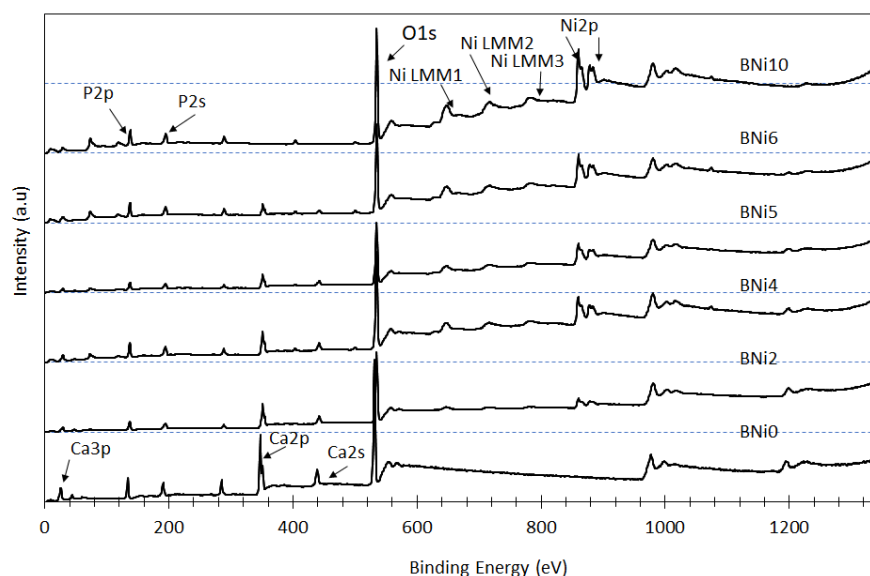


Figure 5. XPS spectra of $\text{Ca}_x\text{Ni}_{1-x}\text{HPO}_4 \cdot n\text{H}_2\text{O}$ compounds.

The effect of the Ni/Ca ratio on the binding energies of Ca 2s, P 2s, and Ni 2p peaks, which are shown in Figure 6A–C, respectively, evidence that increasing the Ni/Ca molar ratio from 0 to 0.25 (BNi2) results in an increase in the binding energies of the Ca 2s and P 2s peaks: from 438 to 442 eV and from 190 to 194 eV, respectively. In turn, the findings pertaining to sample BNi10 show that the binding energies of Ca 2s and P 2s remain relatively stable once nearly 100% of Ca is replaced by Ni.

The analyses also indicate that as the Ni/Ca ratio increases to 0.67 (BNi4), to 1 (BNi5), and further to 1.5 (BNi6), the intensity of the Ni 2p peak markedly increases—likewise to be expected, since the rate of replacement of Ca with Ni is accompanied by the precipitation of hexaaquanickel(II) hydrogenphosphate monohydrate. As confirmed by the XRD pattern shown in Figure 1, BNi4 is the first compound formed that contains HNiP crystals, while BNi10 comprises only pure hexaaquanickel(II) hydrogenphosphate monohydrate and thus produces Ni 2p and Ni Auger peaks of the highest intensity.

In sum, the XPS results reported above confirm that when the Ni/Ca ratio in the starting solution is low, Ca is partially replaced by Ni, but this is sufficient to alter the crystal structure of the $\text{Ca}_x\text{Ni}_{1-x}\text{HPO}_4 \cdot n\text{H}_2\text{O}$ compounds by increasing the binding energies of Ca 2s and P 2s peaks [41]. As the Ni concentration increases with the decrease in Ca concentration, supersaturation decreases (increases) with respect to brushite (hexaaquanickel(II) hydrogenphosphate monohydrate). Consequently, pure HNiP is obtained when no Ca is present in the system, as is the case for the BNi10 compound.

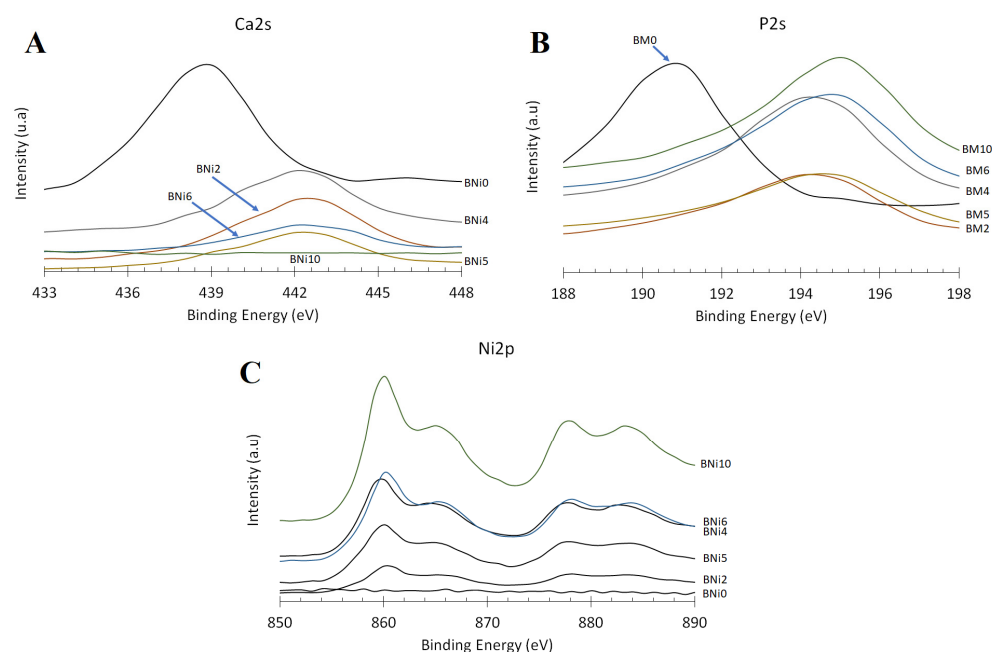


Figure 6. XPS analysis of the chemical state of (A) Ca 2s, (B) P 2s, and (C) Ni 2p orbitals in $\text{Ca}_x\text{Ni}_{1-x}\text{HPO}_4 \cdot n\text{H}_2\text{O}$ compounds.

3.3. Thermogravimetric Analysis (TGA)

The TGA results for all analyzed compounds (BNi0 to BNi10) are shown in Figure 7. Brushite has a crystal structure made up of compact sheets formed by parallel chains in which Ca ions are coordinated by six phosphate ions and two oxygen atoms belonging to the water molecules, making it a water-bearing phosphate [9]. Moreover, two sharp peaks reflect the mass loss as a result of heating from 80 to 220 °C. Brushite is characterized by two water molecules in its lattice and adsorbed water molecules on its surface [42,43]. Available evidence indicates that some of the chemically-bound water is released as brushite transforms to monetite (CaHPO_4) at ≈ 220 °C [44] and further to calcium pyrophosphate ($\text{Ca}_2\text{P}_2\text{O}_7$) as the temperature increases to ≈ 440 °C [8]. According to our results, when pure brushite (BNi0) is heated to 750 °C, approximately 21 wt % of its mass is lost [10], which is comparable to the theoretical mass loss of 20.93 wt % [45]. The BNi2–BNi6 samples with progressively greater Ni/Ca ratios lose more mass (27–35%), while a mass loss of 31.5 wt % is obtained for BNi10 containing solely hexaaquanickel(II) hydrogenphosphate monohydrate.

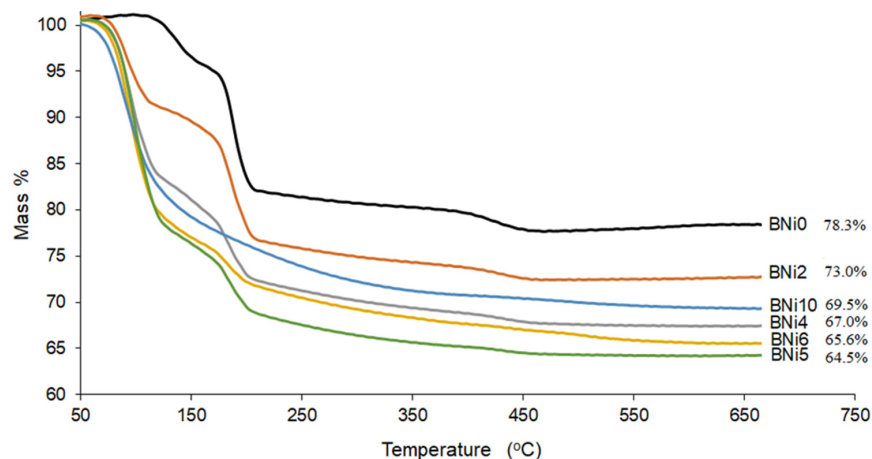
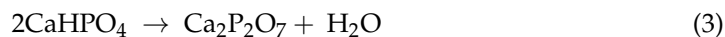
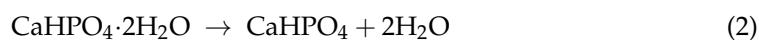


Figure 7. TG curves of $\text{Ca}_x\text{Ni}_{1-x}\text{HPO}_4 \cdot n\text{H}_2\text{O}$ compounds (product names Bni0–Bni10).

The brushite dehydration reaction is provided in Equation (2), while the formation of calcium pyrophosphate is described in Equation (3).



The mass-loss rate for $\text{Ca}_x\text{Ni}_{1-x}\text{HPO}_4 \cdot n\text{H}_2\text{O}$ compounds as a function of temperature is shown in Figure 8. In Figure 8A–E, the dehydration peaks corresponding to the two water molecules of pure brushite (BNi0) are evident, and they are accompanied by the peaks characterizing the compounds obtained when the Ni/Ca ratio increased from 0.25 (BNi2) to 1.5 (BNi6). As indicated previously [24], partial replacement of Ca by Ni is initially accompanied by limited production of hexaaquanickel(II) hydrogenphosphate monohydrate. However, when the Ca is fully replaced by Ni in the starting solution (BNi10, Figure 8F), a primary zone of mass loss corresponding to HNiP is obtained at approximately 93 °C.

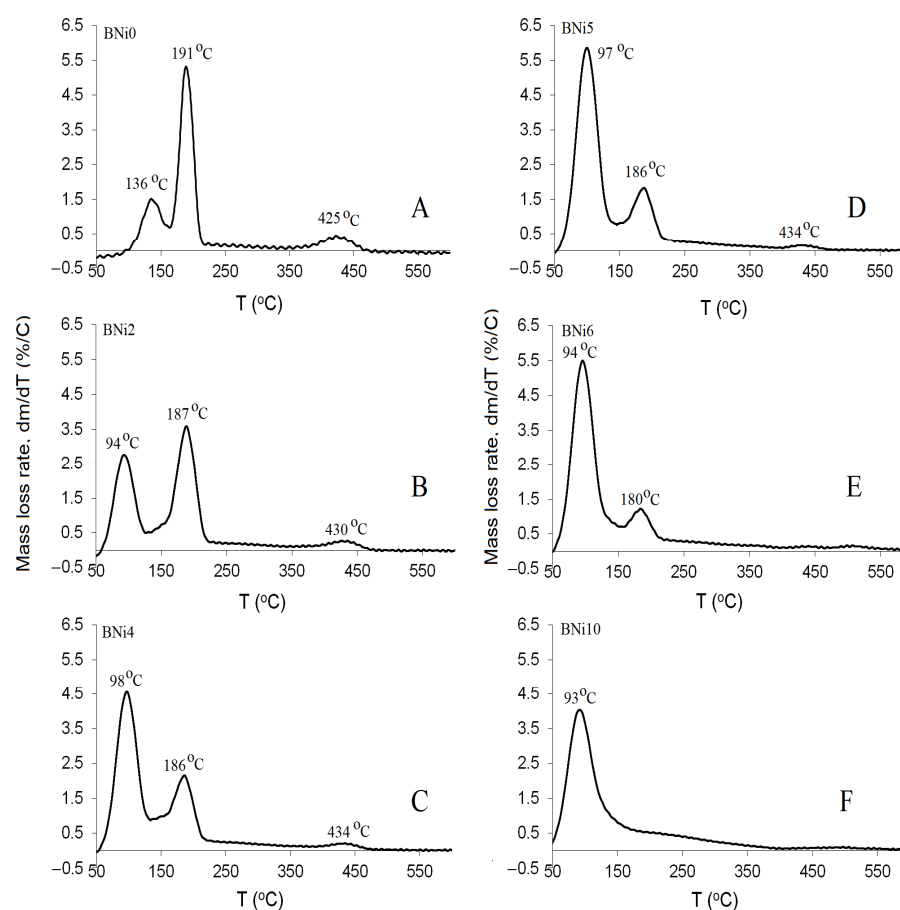


Figure 8. Differential TGA of diverse $\text{Ca}_x\text{Ni}_{1-x}\text{HPO}_4 \cdot n\text{H}_2\text{O}$ compounds: (A) BNi0; (B) BNi2; (C) BNi4; (D) BNi5; (E) BNi6, and (F) BNi10.

3.4. Phase Evolution during the Precipitation of $\text{Ca}_x\text{Ni}_{1-x}\text{HPO}_4 \cdot n\text{H}_2\text{O}$ Compounds

The results obtained in the present study indicate that the original shape of plate-like brushite crystals is preserved when the Ni/Ca ratio in the starting solution does not exceed 0.25 [39]. On the other hand, their size decreases due to the presence of Ni, as nickel inhibits crystal growth [20].

When the Ni/Ca ratio increases to 0.25 and even to 1.5 (BNi4–BNi6), HNiP with orthorhombic crystals starts to precipitate and eventually remains as the only phase when

the Ni/Ca ratio increases further (with nano-scale crystals of approximately 500 nm size, as shown in Table 4).

Table 4. Phase evolution, crystal size, and structure as a function of the Ni/Ca molar ratio in solution.

Ni/Ca Ratio	Crystal Structure	Crystal Size (μm)	Compounds Formed
$0 < 0.25$	Monoclinic	~ 10	Brushite
$0.25 \leq x \leq 1.5$	Monoclinic/orthorhombic	$\sim 5 + 0.5$	Brushite + HNiP
> 1.5	Orthorhombic	~ 0.5	HNiP

4. Conclusions

In this study, the degree of replacement of Ca by Ni in brushite was investigated by examining a range of $\text{Ca}_x\text{Ni}_{1-x}\text{HPO}_4 \cdot n\text{H}_2\text{O}$ biomaterials that were subjected to XRD, SEM, XPS, FTIR, and TG analysis.

This study is consistent with previous studies [24], where the substitution of Ca^{2+} with Ni^{2+} by 20% or more leads to the formation of a mixture of compounds. The findings indicate that when the Ni/Ca molar ratio gradually increases to 1.5 (whereby the solution supersturation with respect to Ni increases), both monoclinic Brushite and nanocrystals of orthorhombic HNiP precipitate. This study puts forth a novel procedure for HNiP synthesis (BNi10), utilizing the precipitation method. While brushite is considered a biomaterial precursor and a source of Ca ions, HNiP could be a promising compound as a source of Ni ions.

These insights might be valuable for the future synthesis of biomaterials with specific composition and properties, as they indicate that by controlling the Ni/Ca ratio in the starting solution, a variety of material compositions and morphologies can be attained. However, additional studies are required to assess the performance of the produced biomaterials, focusing specifically on their biological and mechanical aspects as well as physicochemical and antibacterial properties. The effect of doping with additional ions should also be investigated in depth, given that Ni may exhibit both beneficial and detrimental effects upon the biomaterials aimed for medical applications (such as kidney stone treatment and bone tissue engineering).

Author Contributions: Conceptualization, M.A. and K.I.; methodology, M.A.; validation, M.A., K.I. and A.S.A.; formal analysis, A.A.A. and A.E.; investigation, A.S.A. and M.A.; resources, M.E.M.; data curation, A.E. and A.A.A.; writing—original draft preparation, M.A.; writing—review and editing, T.F.Q.; visualization, M.A.; supervision, M.A., M.E.M. and T.F.Q. All authors have read and agreed to the published version of the manuscript.

Funding: This research received no external funding.

Institutional Review Board Statement: Not applicable.

Informed Consent Statement: Not applicable.

Data Availability Statement: Not applicable.

Conflicts of Interest: The authors declare no conflict of interest.

References

- Boanini, E.; Silingardi, F.; Gazzano, M.; Bigi, A. Synthesis and Hydrolysis of Brushite (DCPD): The Role of Ionic Substitution. *Cryst. Growth Des.* **2021**, *21*, 1689–1697. [[CrossRef](#)]
- Radwan, N.H.; Nasr, M.; Ishak, R.A.; Abdeltawab, N.F.; Awad, G.A. Chitosan-calcium phosphate composite scaffolds for control of postoperative osteomyelitis: Fabrication, characterization, and in vitro–in vivo evaluation. *Carbohydr. Polym.* **2020**, *244*, 116482. [[CrossRef](#)] [[PubMed](#)]
- Alshaar, M.; Abdel-Fattah, E.; Saadeddin, I.; Al Battah, F.; Issa, K.I.; Saffarini, G. The effect of natural fibres template on the chemical and structural properties of Biphasic Calcium Phosphate scaffold. *Mater. Res. Express* **2020**, *7*, 065405. [[CrossRef](#)]

4. Cirillo, M.; Martelli, G.; Boanini, E.; Rubini, K.; Di Filippo, M.; Torricelli, P.; Pagani, S.; Fini, M.; Bigi, A.; Giacomini, D. Strontium substituted hydroxyapatite with β -lactam integrin agonists to enhance mesenchymal cells adhesion and to promote bone regeneration. *Colloids Surf. B Biointerfaces* **2021**, *200*, 111580. [[CrossRef](#)] [[PubMed](#)]
5. Khalifehzadeh, R.; Arami, H. Biodegradable calcium phosphate nanoparticles for cancer therapy. *Adv. Colloid Interface Sci.* **2020**, *279*, 102157. [[CrossRef](#)]
6. Shyong, Y.-J.; Chang, K.-C.; Lin, F.-H. Calcium phosphate particles stimulate exosome secretion from phagocytes for the enhancement of drug delivery. *Colloids Surf. B Biointerfaces* **2018**, *171*, 391–397. [[CrossRef](#)]
7. Liu, Y.; Ma, R.; Li, D.; Qi, C.; Han, L.; Chen, M.; Fu, F.; Yuan, J.; Li, G. Effects of calcium magnesium phosphate fertilizer, biochar and spent mushroom substrate on compost maturity and gaseous emissions during pig manure composting. *J. Environ. Manag.* **2020**, *267*, 110649. [[CrossRef](#)]
8. Revelo, C.F.; Colorado, H.A. A green composite material of calcium phosphate cement matrix with additions of car tire waste particles. *Int. J. Appl. Ceram. Technol.* **2021**, *18*, 182–191. [[CrossRef](#)]
9. Huertas, C.F.R.; Vieira, C.M.F.; Colorado, H.A. A hybrid composite for structural applications made of rubber waste tires and calcium phosphate cement. *Int. J. Appl. Ceram. Technol.* **2021**, *18*, 1342–1353. [[CrossRef](#)]
10. Boehm, A.V.; Meiningner, S.; Gbureck, U.; Müller, F.A. Self-healing capacity of fiber-reinforced calcium phosphate cements. *Sci. Rep.* **2020**, *10*, 9430. [[CrossRef](#)]
11. Das, K.K.; Das, S.N.; Dhundasi, S.A. Nickel, its adverse health effects & oxidative stress. *Indian J. Med. Res.* **2008**, *128*, 412–425. [[PubMed](#)]
12. Priya, B.A.; Senthilguru, K.; Agarwal, T.; Narayana, S.N.G.H.; Giri, S.; Pramanik, K.; Pal, K.; Banerjee, I. Nickel doped nanohydroxyapatite: Vascular endothelial growth factor inducing biomaterial for bone tissue engineering. *RSC Adv.* **2015**, *5*, 72515–72528. [[CrossRef](#)]
13. Salnikow, K.; An, W.G.; Melillo, G.; Blagosklonny, M.V.; Costa, M. Nickel-induced transformation shifts the balance between HIF-1 and p53 transcription factors. *Carcinogenesis* **1999**, *20*, 1819–1823. [[CrossRef](#)] [[PubMed](#)]
14. Civjan, S.; Huget, E.F.; DeSimon, L.B. Potential Applications of Certain Nickel-Titanium (Nitinol) Alloys. *J. Dent. Res.* **1975**, *54*, 89–96. [[CrossRef](#)]
15. Fini, M.; Aldini, N.N.; Torricelli, P.; Giavaresi, G.; Borsari, V.; Lenger, H.; Bernauer, J.; Giardino, R.; Chiesa, R.; Cigada, A. A new austenitic stainless steel with negligible nickel content: An in vitro and in vivo comparative investigation. *Biomaterials* **2003**, *24*, 4929–4939. [[CrossRef](#)]
16. Sayahi, M.; Santos, J.; El-Feki, H.; Charvillat, C.; Bosc, F.; Karacan, I.; Milthorpe, B.; Drouet, C. Brushite (Ca,M)HPO₄ · 2H₂O doping with bioactive ions (M = Mg²⁺, Sr²⁺, Zn²⁺, Cu²⁺, and Ag⁺): A new path to functional biomaterials? *Mater. Today Chem.* **2020**, *16*, 100230. [[CrossRef](#)]
17. Alkhraisat, M.H.; Rueda, C.; Cabarcos, E.L. Strontium Ions Substitution in Brushite Crystals: The Role of Strontium Chloride. *J. Funct. Biomater.* **2011**, *2*, 31–38. [[CrossRef](#)]
18. Xue, Z.; Wang, Z.; Sun, A.; Huang, J.; Wu, W.; Chen, M.; Hao, X.; Huang, Z.; Lin, X.; Weng, S. Rapid construction of polyetheretherketone (PEEK) biological implants incorporated with brushite (CaHPO₄ · 2H₂O) and antibiotics for anti-infection and enhanced osseointegration. *Mater. Sci. Eng. C* **2020**, *111*, 110782. [[CrossRef](#)]
19. Kim, Y.; Lee, S.Y.; Roh, Y.; Lee, J.; Kim, J.; Lee, Y.; Bang, J.; Lee, Y.J. Optimizing Calcium Phosphates by the Control of pH and Temperature via Wet Precipitation. *J. Nanosci. Nanotechnol.* **2015**, *15*, 10008–10016. [[CrossRef](#)]
20. Alshaaq, M.; Al-Kafawein, J.; Qazaq, A.; Issa, K.; Saffarini, G. Effects of magnetite incorporation in a chemically bonded phosphate ceramic. *J. Phys. Chem. Solids* **2022**, *162*, 110531. [[CrossRef](#)]
21. Luo, J.; Engqvist, H.; Persson, C. A ready-to-use acidic, brushite-forming calcium phosphate cement. *Acta Biomater.* **2018**, *81*, 304–314. [[CrossRef](#)] [[PubMed](#)]
22. Mert, I.; Mandel, S.; Tas, A.C. Do cell culture solutions transform brushite (CaHPO₄ · 2H₂O) to octacalcium phosphate (Ca₈(HPO₄)₂(PO₄)₄ · 5H₂O)? In *Advances in Bioceramics and Porous Ceramics IV*; Narayan, R., Colombo, P., Eds.; John Wiley & Sons, Inc.: Hoboken, NJ, USA, 2011; pp. 79–94.
23. Hurle, K.; Oliveira, J.; Reis, R.; Pina, S.; Goetz-Neunhoffer, F. Ion-doped Brushite Cements for Bone Regeneration. *Acta Biomater.* **2021**, *123*, 51–71. [[CrossRef](#)] [[PubMed](#)]
24. Guerra-López, J.R.; Güida, J.A.; Ramos, M.A.; Punte, G. The influence of nickel on brushite structure stabilization. *J. Mol. Struct.* **2017**, *1137*, 720–724. [[CrossRef](#)]
25. Guerra-López, J.; Güida, J.; Bianchi, A.; Punte, G. Influence of carbonate and nickel(II) concentration on the synthesis of calcium phosphates. *J. Solid State Chem.* **2018**, *267*, 98–105. [[CrossRef](#)]
26. Patil, S.B.; Jena, A.; Bhargava, P. Influence of Ethanol Amount During Washing on Deagglomeration of Co-Precipitated Calcined Nanocrystalline 3YSZ Powders. *Int. J. Appl. Ceram. Technol.* **2012**, *10*, E247–E257. [[CrossRef](#)]
27. Piva, R.H.; Piva, D.H.; Pierri, J.; Montedo, O.R.K.; Morelli, M.R. Azeotropic distillation, ethanol washing, and freeze drying on coprecipitated gels for production of high surface area 3Y-TZP and 8YSZ powders: A comparative study. *Ceram. Int.* **2015**, *41*, 14148–14156. [[CrossRef](#)]
28. Lu, B.-Q.; Willhammar, T.; Sun, B.-B.; Hedin, N.; Gale, J.D.; Gebauer, D. Introducing the crystalline phase of dicalcium phosphate monohydrate. *Nat. Commun.* **2020**, *11*, 1546. [[CrossRef](#)]

29. Alshaer, M.; Afify, A.S.; Moustapha, M.E.; Hamad, N.; Hammouda, G.A.; Rocha, F. Effects of the full-scale substitution of strontium for calcium on the microstructure of brushite: $(\text{Ca}_x\text{Sr}_{1-x})\text{HPO}_4 \cdot n\text{H}_2\text{O}$ system. *Clay Miner.* **2020**, *55*, 366–374. [[CrossRef](#)]
30. Nosrati, H.; Le, D.Q.S.; Emameh, R.Z.; Perez, M.C.; Bünger, C.E. Nucleation and growth of brushite crystals on the graphene sheets applicable in bone cement. *Bol. Soc. Esp. Cerám. Vidr.* **2022**, *61*, 27–34. [[CrossRef](#)]
31. Wu, F.; Wei, J.; Guo, H.; Chen, F.; Hong, H.; Liu, C. Self-setting bioactive calcium–magnesium phosphate cement with high strength and degradability for bone regeneration. *Acta Biomater.* **2008**, *4*, 1873–1884. [[CrossRef](#)]
32. Alshaer, M.; Issa, K.; Alanazi, A.; Mallouh, S.; Afify, A.; Moustapha, M.; Komnitsas, K. Gradual Replacement of Ca^{2+} with Mg^{2+} Ions in Brushite for the Production of $\text{Ca}_{1-x}\text{Mg}_x\text{HPO}_4 \cdot n\text{H}_2\text{O}$ Materials. *Minerals* **2021**, *11*, 284. [[CrossRef](#)]
33. Alshaer, M.; Al-Kafawein, J.; Afify, A.S.; Hamad, N.; Saffarini, G.; Issa, K. Effect of Ca^{2+} Replacement with Cu^{2+} Ions in Brushite on the Phase Composition and Crystal Structure. *Minerals* **2021**, *11*, 1028. [[CrossRef](#)]
34. Giriskan, G.; Tas, A.C. Development of biomineralization solutions to facilitate the transformation of brushite ($\text{CaHPO}_4 \cdot 2\text{H}_2\text{O}$) into octacalcium phosphate ($\text{Ca}_8(\text{HPO}_4)_2(\text{PO}_4)_4 \cdot 5\text{H}_2\text{O}$). In Proceedings of the 15th National Biomedical Engineering Meeting (BIYOMUT), Antalya, Turkey, 21–24 April 2010.
35. Tamimi, F.; Le Nihouannen, D.; Eimar, H.; Sheikh, Z.; Komarova, S.; Barralet, J.; Tamimi, F. The effect of autoclaving on the physical and biological properties of dicalcium phosphate dihydrate bioceramics: Brushite vs. monetite. *Acta Biomater.* **2012**, *8*, 3161–3169. [[CrossRef](#)] [[PubMed](#)]
36. Madhurambal, G.; Subha, R.; Mojumdar, S.C. Crystallization and thermal characterization of calcium hydrogen phosphate dihydrate crystals. *J. Therm. Anal.* **2009**, *96*, 73–76. [[CrossRef](#)]
37. Rajendran, K.; Keefe, C.D. Growth and characterization of calcium hydrogen phosphate dihydrate crystals from single diffusion gel technique. *Cryst. Res. Technol.* **2010**, *45*, 939–945. [[CrossRef](#)]
38. Eldrehmy, E.; Alghamdi, Y.; Amer, H.; Yassin, M.; Mostafa, S.; Moustapha, M.E.; Menazea, A. Hydroxyapatite-based bio-ceramic of ternary nanocomposites containing cuprous oxide/graphene oxide for biomedical applications. *Diam. Relat. Mater.* **2022**, *126*, 109121. [[CrossRef](#)]
39. Septiani, N.L.W.; Kaneti, Y.V.; Fathoni, K.B.; Wang, J.; Ide, Y.; Yulianto, B.; Nugraha; Dipojono, H.K.; Nanjundan, A.K.; Golberg, D.; et al. Self-assembly of nickel phosphate-based nanotubes into two-dimensional crumpled sheet-like architectures for high-performance asymmetric supercapacitors. *Nano Energy* **2019**, *67*, 104270. [[CrossRef](#)]
40. Chen, Z.; Zhou, D.; Gao, T.; Shen, W.; Dong, X.; Naito, S.; Qin, L.; Huang, Y. Unusual adsorption and desorption behaviors of NO and CO on nanoporous nickel phosphate VSB-5: In situ FT-IR and TPD study. *Catal. Today* **2015**, *258*, 199–204. [[CrossRef](#)]
41. Huang, H.; Li, J.; Li, B.; Zhang, D.; Zhao, N.; Tang, S. Comparison of different K-struvite crystallization processes for simultaneous potassium and phosphate recovery from source-separated urine. *Sci. Total Environ.* **2019**, *651*, 787–795. [[CrossRef](#)]
42. Gashti, M.P.; Stir, M.; Hulliger, J. Growth of strontium hydrogen phosphate/gelatin composites: A biomimetic approach. *New J. Chem.* **2016**, *40*, 5495–5500. [[CrossRef](#)]
43. Tortet, L.; Gavarrri, J.R.; Nihoul, G.; Dianoux, A. Study of Protonic Mobility in $\text{CaHPO}_4 \cdot 2\text{H}_2\text{O}$ (Brushite) and CaHPO_4 (Monetite) by Infrared Spectroscopy and Neutron Scattering. *J. Solid State Chem.* **1997**, *132*, 6–16. [[CrossRef](#)]
44. Dosen, A.; Giese, R.F. Thermal decomposition of brushite, $\text{CaHPO}_4 \cdot 2\text{H}_2\text{O}$ to monetite CaHPO_4 and the formation of an amorphous phase. *Am. Mineral.* **2011**, *96*, 368–373. [[CrossRef](#)]
45. Frost, R.L.; Palmer, S.J. Thermal stability of the ‘cave’ mineral brushite $\text{CaHPO}_4 \cdot 2\text{H}_2\text{O}$ —Mechanism of formation and decomposition. *Thermochim. Acta* **2011**, *521*, 14–17. [[CrossRef](#)]